metals

MDPI

Article

Influence of the Miniaturisation Effect on the Effective Stiffness of Lattice Structures in Additive Manufacturing

Guillaume Meyer [1,*], Florian Brenne [2,3], Thomas Niendorf [2] and Christian Mittelstedt [1]

[1] Konstruktiver Leichtbau und Bauweisen, Department of Mechanical Engineering, Technische Universität Darmstadt, Otto-Berndt-Straße 2, 64287 Darmstadt, Germany; christian.mittelstedt@klub.tu-darmstadt.de

[2] Institut für Werkstofftechnik, Universität Kassel, Mönchebergstraße 3, 34125 Kassel, Germany; fbrenne@illinois.edu (F.B.); niendorf@uni-kassel.de (T.N.)

[3] Department of Mechanical Science and Engineering, University of Illinois at Urbana-Champaign, 1206 W Green St, Urbana, IL 61801, USA

* Correspondence: guillaume.meyer@klub.tu-darmstadt.de; Tel.: +49-(0)6151-16-22025

Received: 25 September 2020; Accepted: 23 October 2020; Published: 29 October 2020

Abstract: Thin-walled and cellular structures are characterised by superior lightweight potential due to their advantageous stiffness to weight ratio. They find particular interest in the field of additive manufacturing due to robust and reproducible manufacturability. However, the mechanical performance of such structures strongly depends on the manufacturing process and resultant geometrical imperfections such as porosity, deviations in strut thickness or surface roughness, for which an understanding of their influence is crucially needed. So far, many authors conducted empirical investigations, while analytical methods are rarely applied. In order to obtain efficient design rules considering both mechanical properties and process induced characteristics, analytical descriptions are desirable though. Available analytical models for the determination of effective properties are mostly based on the simple advancement of beam theories, mostly ignoring manufacturing characteristics that, however, strongly influence the mechanical properties of additive manufactured thin-walled structures. One example is the miniaturisation effect, a microstructural effect that has been identified as one of the main drivers of the effective elasto-plastic properties of lightweight structures processed by additive manufacturing. The current work highlights the need to quantify further microstructural effects and to encourage combining them into mesostructural approaches in order to assess macrostructural effective properties. This multi-scale analysis of lattice structures is performed through a comparison between effective stiffness calculated through an analytical approach and compression tests of lattice structures, coupled with an investigation of the arrangement of their struts. In order to cover different potential loading scenarios, bending-dominated and stretch-dominated lattice structures made of the commonly used materials 316L and Ti6Al4V are considered, whereby the impact of microstructural phase transformation during processing is taken into account.

Keywords: additive manufacturing; lightweight design; lattice structures; miniaturisation effect; microstructure

1. Introduction

Additive manufacturing, i.e., the 3D-printing technology, has found application in several industries, especially due to its flexibility and versatility enabling the realization of new design parts that cannot be achieved by the classical manufacturing processes on an economic basis [1,2]. Thanks to its nature, the additive manufacturing process can offer tailored designs based on optimised geometries as an integral product, allowing a reduction of the single parts number and manufacturing

steps involved in comparison to classical construction methods. This is where the concepts of "individualization for free" and "complexity for free" are derived from. These concepts, schematically shown in Figure 1, are particularly relevant for the lightweight industry, with aeronautical and automotive engineering being the most prominent branches, where weight, mechanical performance and, most importantly, costs are the driving selection criteria. However, the main challenge of the additive manufacturing technology lies in achieving a serial production maturity, i.e., reliable and reproducible provision of subsequently mechanically loaded parts with little rework, the latter being a time and cost consuming factor [3]. The main concern here is related to the process dependent performance of additively manufactured components. In this regard, one key issue is the lack of certification standards [4]. This aspect highlights the prevailing lack of control over the additive manufacturing technology being a major roadblock to its widespread use. The immense potential of the technology, however, when exploited to its greatest extent, could provide a breakthrough in many fields related to lightweight engineering.

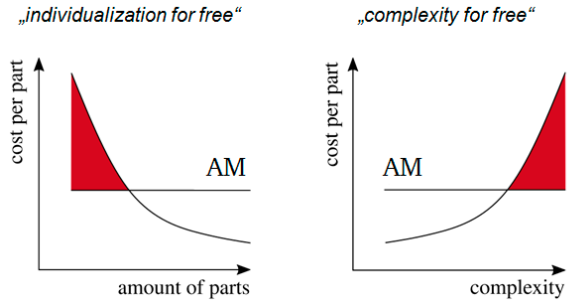

Figure 1. Advantages of additive manufacturing (horizontal lines) in terms of industrial application as compared to conventional manufacturing (reference curves) [5].

This statement is particularly true for lattice structures [6], which are still not implemented in lightweight load carrying structures, even if application is highly promising. Predictive modelling of such structures is the main challenge here. Available analytical models [7–11] are subject to relatively high deviations from experiments [12] due to modelling assumptions that do not take into account the systematic manufacturing defects [13,14]. Alternative approaches try to follow a more pragmatic approach, i.e., based on semi-empirical finite element models to account for manufacturing parameters and their influence on resulting lattice quality, mechanical performance is predicted [15]. Based on these models, appropriate processing windows were established [16–19]. Defects that are typically taken into account are pores and geometrical inaccuracy of individual struts [13,14,20]. These have a major impact especially on mechanical properties at large deformations. The microstructural arrangement has been identified as potential driving factor for experimental deviations; however, most of the focus is only on grain morphology while the texture is not considered. This statement is quite surprising taking into account that the influence of process parameters on microstructure evolution of additive manufactured bulk material is non-negligible [21–28]. Based on data obtained from many different alloys, the melting and the subsequent solidification process have been identified as the dominant factors for final appearance of the resulting grain morphology and texture. Apart from the cooling rate, which depends mainly on the size of the melting pool, the direction of the temperature gradient, i.e., a vector strongly affected by the melting pool shape, is of significant relevance. It has been proven that it is possible to directly design properties, e.g., by establishing microstructures with strong <001> texture parallel to the build direction. Additive manufacturing of thin walled structures and, in particular, lattice structures lead to an exposure of small cross sections only. Depending on the overall build layout, this can eventually lead to minimization of time intervals between melting of two layers and, most importantly, strongly directed heat flux. It is, thus, reasonable to assume that these structures can be considered as being most severely influenced by the process parameters and the build orientation [29–35]. One of the few studies investigating the influence of strut geometry

on microstructure and texture as well as on mechanical properties is that of Wang et al. For 316L stainless steel struts, the texture changes from a strong <100> to a <110> texture parallel to the build direction as the strut diameter increases. This is accompanied by an increase in strength and ductility [36]. However, the still low number of empirical investigations as well as the lack of systematic development of corresponding statistical approaches implying analytical methods highlights the very limited understanding of the impact of microstructural effects on the macroscopic mechanical behavior and more particularly the stiffness of these 3D-printed structures.

The aim of the present paper is to highlight the impact of the so-called miniaturisation effect, i.e., local texturing due to temperature gradients in lattice struts depending on the process parameters and geometrical input, on the elasto-plastic properties of additively manufactured lattice structures. Understanding this complex interaction between process parameters, microstructures and material properties is essential for prediction of the structural behavior of additive manufactured parts and in particular of thin walled and lattice structures. In the present study, an approach bridging several scales is proposed based on data being recompiled from previous work for the purpose of this investigation [11,35–39]. This contribution is divided into various parts, where experimental and analytical methods are in focus. The first part addresses the influence of process parameters on the microstructural and mechanical properties of bulk material with decreasing diameter. To do so, struts with various diameters were investigated in order to analyse the impact of the strut thickness on the local microstructure by means of Electron Backscatter Diffraction (EBSD). The second part deals with lattice structures and their effective macroscopic mechanical behavior. Due to the nature of the analytical model employed, only the mechanical properties in the linear elastic domain were contemplated, i.e., the effective stiffness. The macroscopic deformation behavior was evaluated by comparing the effective compressive stiffness obtained from experimental data and the model predictions. The local deformation behavior, i.e., the loading state of each strut in both types of lattice structures, was additionally assessed to substantiate findings. Both macroscopic and microscopic deformation behavior were analysed via digital image correlation (DIC).

2. Materials and Methods

The non-stochastic porous structures investigated in this paper were body-centred cubic (bcc) and double face centred cubic (f2ccz) lattices, which are representatives of bending-dominated and stretch-dominated structures, respectively. Materials in focus were AISI 316L stainless steel and Ti6Al4V titanium alloy, two commonly used materials, especially in additive manufacturing and lightweight engineering. The main differences of these alloys—in the context of the current study—are their respective ductilities (high for 316L, low for Ti6Al4V) and the phase evolution upon solidification and cooling, i.e., 316L being single phase (face centred cubic austenite) only upon solidification, while Ti6Al4V shows a phase transformation from a body centred cubic high-temperature phase to a hexagonal crystal structure or a martensitic phase, respectively, depending on cooling rate. Upon additive manufacturing and selective laser melting in particular, the martensitic phase is found to be absolutely dominant in the as-built condition [37].

The powder used for additive manufacturing of austenitic steel 316L and the Ti6Al4V alloy was processed by electrode induction-melting gas atomization. The nominal chemical composition of both alloys can be found in Table 1.

The particle size distributions used for selective laser melting ranged from 20 µm to 63 µm for Ti6Al4V and from 10 µm to 45 µm for 316L. Powders used are depicted in the micrographs obtained by scanning electron microscopy (SEM), Figure 2. The titanium alloy powder is characterised by an almost perfect spherical shape with only very few satellites being attached, while significantly more irregularities can be seen in case of the 316L powder.

In order to isolate the miniaturisation effect being in focus of this investigation, deviation in surface roughness and geometrical accuracy, respectively, is avoided by selecting only one specific build orientation and one parameter set. It is then assumed that, for the same printing quality, the only factor

affecting the effective stiffness of lattice structures is local differences in texture, whereby other defects are expected to lead to difficulties in identifying the elastic range of the experimental results. Since all specimens were manufactured upright, their longitudinal axis is therefore parallel to the build direction (BD) and, in the case of the lattice structures, corresponds to the loading direction (LD). The specimens were manufactured using the laser powder bed fusion (L-PBF) technology, which comprises layer-wise deposition and melting of metal powders.

Table 1. Nominal chemical composition of the 316L and Ti6Al4V powders in weight-%.

316L	Fe	Cr	Ni	Mo	C	Si	Mn	
	Rest	16.5–18.5	10–13	2–2.5	<0.03	<1	<2	
Ti-6Al-4V	Ti	Al	V	Fe	O	C	N	H
	Rest	5.5–6.5	3.4–4.5	<0.25	<0.13	<0.08	<0.05	<0.012

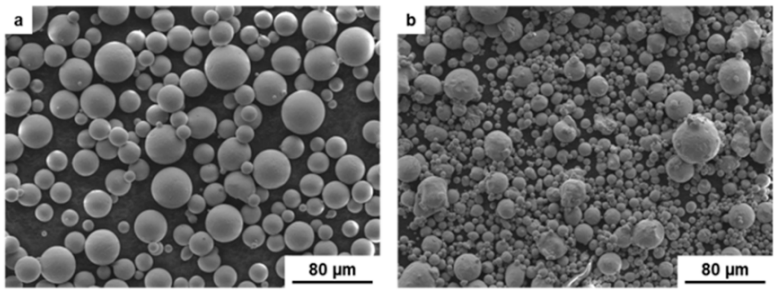

Figure 2. SEM micrographs of powders, (**a**) Ti6Al4V; (**b**) 316L [35].

In order to analyse the influence of geometrical dimensions on the resulting microstructure, cylindrical specimens from 316L having diameters of 0.65 mm, 1.1 mm, 3.1 mm and 5 mm were produced. The manufacturing process parameters, following those used for bulk grip section, are listed in Table 2.

For testing under compressive loading, bcc and f2ccz lattice structures were produced, each being made of 5 × 5 × 5 base cells with 2 mm cell size. Previous studies [37,40] already revealed that these dimensions are sufficient for testing and comparison to real components as number of cells used in lightweight components such as sandwich panels at least in one dimension is not significantly higher. Bulk grip sections were designed at the top and the bottom of the lattice structures for load application and mounting in the test machine, respectively. Both base cells as well as an exemplary test specimen are shown in Figure 3.

In order to allow for robust manufacturing of the lattice test specimens, both beam offset compensation and contour exposure were deactivated. The employed manufacturing process parameters are listed in Table 3. While 316L specimens were tested in the as-built condition only (as the overall properties were shown to be already sufficient for application, i.e., high strength and good ductility), some specimens of the Ti6Al4V alloy were subjected to a two-hour vacuum heat treatment at 1050 °C. The post-treatment provided for a certain plastic deformation capability of the otherwise rather brittle Ti-6Al-4V in the as-built condition. The evacuated specimens were put in the pre-preheated oven, remained for two hours at 1050 °C followed by oven cooling. Subsequent mechanical testing of the Ti6Al4V specimens was consequently done in as-built and heat-treated conditions.

For microstructural characterization, the cylindrical specimens were embedded in resin and mechanically ground until half of the diameter was removed (using grit sizes down to 5 µm). Further polishing was conducted in form of vibropolishing using a suspension with a particle size of 0.04 µm until proper surface finish for subsequent EBSD analysis was achieved. EBSD was conducted using a Phillips XL 40 ESEM TMP (Philips NV, Amsterdam, The Netherlands) in an area of ca. 650 µm × 400 µm

with a step size of 2 µm in the case of the cylinders made from 316L. For the Ti6Al4V that were specimens apart, parameters were employed for EBSD to resolve relevant features of the prevailing microstructure.

Table 2. Process parameters employed for manufacturing of the cylindrical test specimens and the bulk grip section of lattice test specimens.

Material/System	Laser Power (W)	Scan Speed ($mm \cdot s^{-1}$)	Hatch Distance (mm)	Layer Thickness (µm)
316L	175	750	0.12	30
Ti-6Al-4V	175	710	0.12	30

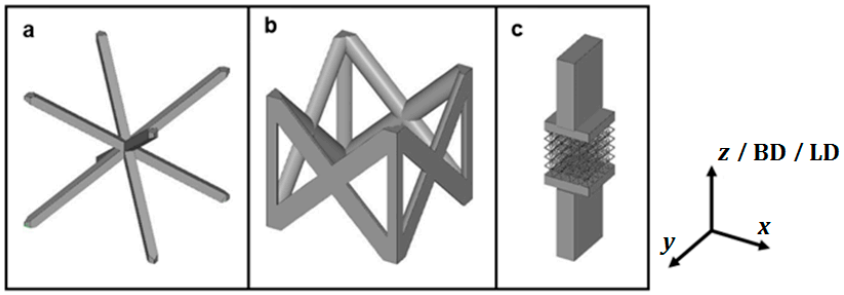

Figure 3. Base cells of the lattice structures, (**a**) bcc; (**b**) f2ccz; (**c**) bcc specimen geometry, recompiled from [35].

Mechanical testing of the lattice structures was done using an MTS 810 servo-hydraulic test rig (MTS System, Minneapolis, MN, USA). The machine operated in displacement control at a crosshead speed of 0.01 $mm \cdot s^{-1}$. Compressive loading was imposed until either a densification of 35% was achieved or a collapse of the majority of struts was observed. The tests were interrupted at regular intervals of 10 µm in order to record images of the specimen surface for analysis of the local strain distribution. For image acquisition a DLSR camera (Nikon D3200, Nikon Corporation, Tokyo, Japan) equipped with a macro lens was used, while commercial halogen spotlights ensured proper illumination of the specimen surface. Image analysis was done by digital image correlation (DIC) using VIC-2D (Correlated Solutions Inc., Irmo, SC, USA).

For comparison purposes, the analytical model described by Souza et al. [11] is exemplarily used. It determines the relationship between aspect ratio, strut diameter, and mechanical properties for a given cellular structure, whereby the cell struts are considered as Timoshenko beams [41] in order to cover high to low aspect ratios. This part of the work focuses on the impact of the aspect ratio of the lattice structure and the resulting Young's moduli. The aspect ratio AR, defined as the relationship of the cell size a and the strut thickness t (Figure 4), is the driver of the lightweight potential of cellular lattice structures. The analytical yield strength is used to determine the limit of the elastic domain in order to assess elastic properties in the experimental part of the investigation.

For the sake of brevity, the way the model works is shortly summed up. Please refer to the corresponding publication for more details [11]. The analytical model consists of a strain energy based homogenization scheme of the representative volume element (RVE) in the linear elastic domain. The RVE is idealized as an ideally homogeneous orthotropic material whose macroscopic strain energy density is determined through an integration of microscopic stresses and strains throughout its complete volume. In order to assess the effective elastic properties, the cell geometry is parametrized and the structural periodicity is granted through the application of boundary conditions. By means of the Castigliano's 2nd theorem and local transformation matrices, the macroscopic strains and stresses can be deducted based on the displacements and forces applied to the RVE. Young's moduli and Poisson's ratios can be obtained as scalar from the uniaxial load case, where a single axial unitary load is considered. The yield strength is then derived from maximal applied loads.

Table 3. Process parameters employed for manufacturing of the lattice structure test specimens.

Material/System	Laser Power (W)	Scan Speed ($mm \cdot s^{-1}$)	Hatch Distance (mm)	Layer Thickness (µm)
316L	175	750	0.12	30
Ti-6Al-4V	175	710	0.12	30

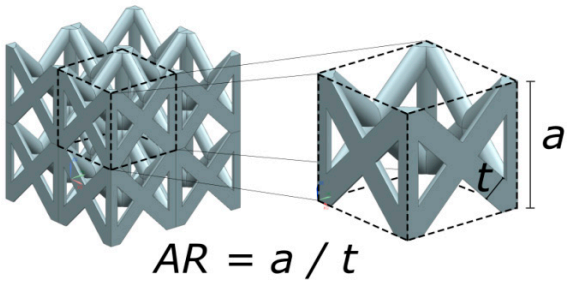

Figure 4. Aspect ratio of cellular lattice structures, exemplarily shown for an f2ccz structure.

The material properties are purposely assumed to be isotropic in the model, even if texture intensities are expected to be relatively high in case of the stainless steel. Used material properties considered are derived from conventionally manufactured material and listed in Table 4.

Table 4. Material properties considered in present work.

Material	E (GPa)	ν (–)
316L [42]	210	0.30
Ti6Al4V [43]	110	0.31

3. Results

3.1. Microstructures

The EBSD mappings (inverse pole figure (IPF) maps) and the corresponding intensity distributions of the IPFs of the cylindrical struts of 316L stainless steel are shown in Figure 5. For all struts, the grain orientations are plotted with respect to BD. The average grain size of the 0.65 mm struts is 90 µm, whereas the struts with higher diameters have average grainsize of about 50 µm. Note that the average grain sizes are related to the diameter of a globular grain of the area of grains seen. In case of the 0.65 mm struts, however, grains are strongly elongated alongside BD with grain dimensions well above 500 µm. The highest texture intensity is observed for the thinnest struts, resembling a strong <001> texture. For increasing strut diameters, the texture intensity decreases and shifts from <001> towards <101>.

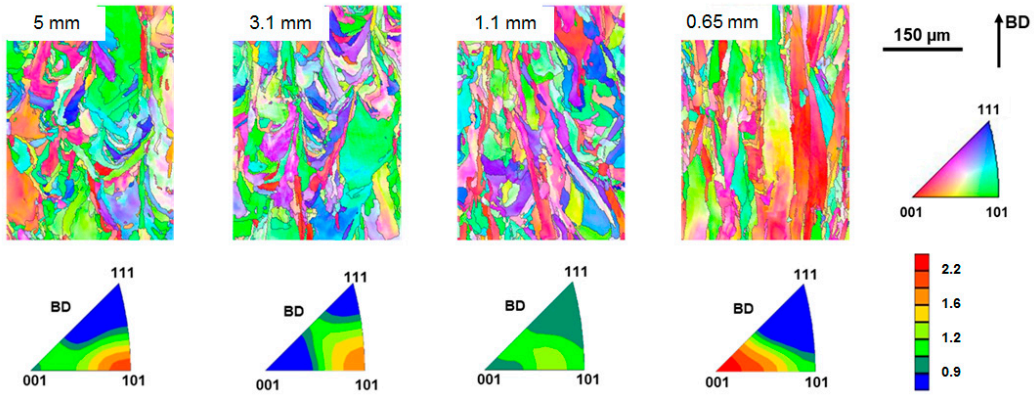

Figure 5. EBSD IPF maps and corresponding IPF intensity plots for BD for 316L steel specimens, recompiled from [38].

In case of the Ti6Al4V bulk material, a very fine grained, martensitic microstructure is observed in the as-built condition (Figure 6a). This is attributable to rapid solidification and cooling, promoting a phase transformation from the β-phase (solidification phase, bcc) being present at high temperatures to the α'-phase (martensite), finally being the dominant phase at room temperature in the as-built condition. Thereby, evolution of the equilibrium phases (Ti6Al4V being a two-phase alloy consisting of the β-phase and the equilibrium hexagonal α-phase) is hindered. As a consequence, the solidification microstructure, as displayed for the 316L in Figure 5, is not perceptible anymore. Thus, in the case of Ti6Al4V, the miniaturisation effects described above do not dominate microstructure and eventually mechanical properties to the same degree as shown for 316L. Moreover, miniaturisation effects can be almost neglected as other microstructural characteristics, e.g., brittleness of the martensite, by far dominate performance [39]. In the course of the heat treatment significant grain coarsening sets in, leading to diameters of individual grains in the range of several hundred micron (Figure 6b). Additionally, the fraction of the β-phase is slightly increased in comparison to the as-built condition, as discussed in detail by Leuders et al. [44]. For bulk material, a higher ductility and reduced strength were reported, eventually effecting the behavior of lattice structures as well [39]. However, if those microstructural changes induced by post-treatment lead to a higher deviation between the predictions of the analytical model and the experimentally observed behavior, cannot be answered at this point and, thus, will be discussed in the remainder of the present study.

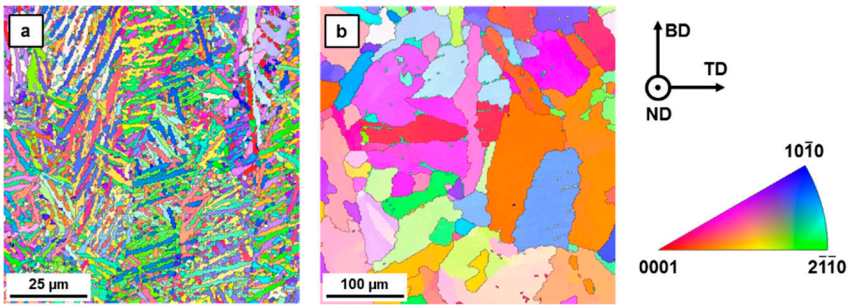

Figure 6. EBSD IPF maps for Ti6Al4V in (**a**) the as-built and (**b**) the heat-treated condition, recompiled from [35].

3.2. Lattice Structures

3.2.1. Local Deformation Behavior

In the present study, the local deformation behavior is analysed in-depth through in-situ compression testing of bcc and f2ccz lattice structures of 316L stainless steel. Results for the Ti6Al4V lattice structures were already published in [39]. For brevity, DIC results are not shown again in the present work, and only the relevant values to be considered for comparison to the results from the modelling approach were extracted from previous data. Figure 7 displays the DIC results revealing the Von-Mises as well as the principal maximal and principal minimal strains at a macroscopic strain of 1%. Due to the very low degree of macroscopic deformation and, thus, presence of merely elastic strains, these strain distributions are characteristic for the lattice types and cell geometries contemplated and, thus, representative irrespective of the material used. A direct comparison between the two materials analysed in the present study was already conducted in [35] and, thus, is not shown here for the sake of brevity.

In Figure 6, the Von-Mises strain plots of the f2ccz lattice specimen (a) indicate that the vertical struts, i.e., the struts parallel to the loading direction, are experiencing highest strains. It can be deduced from the principal strain plots (Figure 7b,c) that the Von-Mises strains are dominated by the minimal principal strains, confirming that the vertical struts are mainly subjected to compressive loading. The presence of tensile loading is nevertheless noticeable in some areas, especially in case of struts with

a 45° orientation towards LD, for which, however, generally low strains are observed. It is important to note that the local Von-Mises strains remain below the applied macroscopic strain of 1%.

The distribution of the Von-Mises strains in the bcc lattice structure (Figure 7d) points at high local concentration of strains in the upper and lower parts of the specimen with local values of up to 2.2%, which is clearly higher than the applied macroscopic strain of 1%. The principal strain plots (Figure 7e,f) show that both the maximum and the minimum principal strains are high, with the positive strains being present on the upper half and the negative strains being observed on the lower half of individual struts. This kind of local strain pattern strongly indicates local bending. With respect to the absolute values derived from the DIC data, it has to be noted that the struts of the bcc structure are inclined with respect to the image plane and, thus, a certain deviation to the actual strains is likely. However, the qualitative strain distribution as well as the comparative assertions made with respect to the f2ccz-structure are seen to be valid.

In order to verify the presence of secondary local effects, vector plots of relevant areas were created. Figure 8 displays vector plots of the maximal principal strains detailing the sections of each lattice structure marked by the red squares in Figure 7b,e.

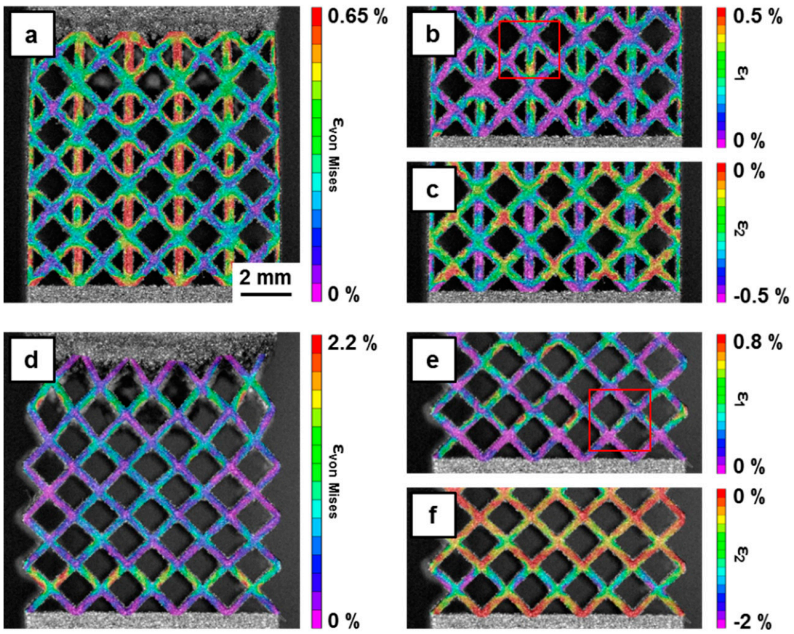

Figure 7. Local strain plots for (**a**–**c**) f2ccz and (**d**–**f**) bcc 316L lattice structures as obtained by DIC at a macroscopic strain of 1%. (**a**,**d**) depict distribution of local Von-Mises strains; (**b**–**f**) highlight maximal and minimal principle strains, respectively—recompiled from [35].

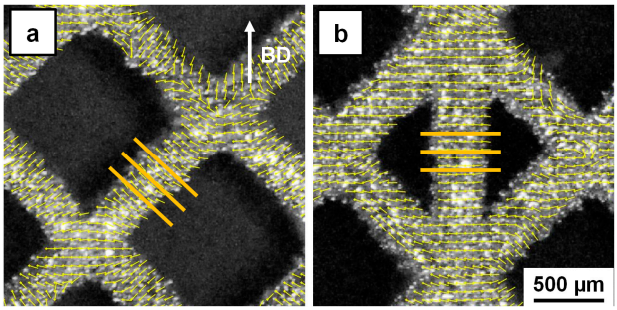

Figure 8. Maximal principal strain vector plots for 316L (**a**) bcc and (**b**) f2ccz lattice structures as obtained by DIC at a macroscopic strain of 1%. The main direction of the vectors is highlighted by the yellow lines in each subimage, the position of the respective sections is highlighted by red squares in Figure 7. The sections of the lattice shown are cropped from the entire structure—recompiled from [35].

The vector plots shown in Figure 8 confirm the dominance of compressive forces in the f2ccz lattice structure (b) and the load carrying behavior of the vertical struts, while diagonal struts seem to have a rather supporting role only. In case of the bcc lattice structure, the positive principal strain vectors in the centre of the struts are perpendicular to the strut axis as well, although a bending component is evident from Figure 7e,f. Thus, the actual load bearing behavior of the bcc structure is seen to be composed of both bending and axial loading components.

3.2.2. Macroscopic Deformation Behavior

The manufactured strut diameters listed in Table 5 were determined based on the raw images recorded for reference purposes for DIC prior to loading. For each investigated configuration, one RVE was measured in terms of cell size and length while all struts being part of this RVE, i.e., four struts for a bcc RVE and five for a f2ccz RVE, were measured three times alongside their length. The heat treatment of the Ti6Al4V specimens had no noticeable impact on the aspect ratio. Thus, the mean aspect ratio values provided for Ti6Al4V lattices are valid for both as-built and heat-treated specimens.

The analytical effective compressive stiffness in the build direction E^*_{ana} is determined using the analytical model. In order to assess the experimental effective compressive stiffness of each lattice structure, a linear approximation of the stress-strain-data (shown in Figure 9) is performed. The extrapolation is based on the stress interval corresponding to 10% to 40% of the analytical yield stress σ^*_{yield} values, shown in Table 6. This rather small interval was chosen in order to avoid the influence of settling effects of the lattice structure, which can already occur at a relatively small strain level, and to ensure that local plastic deformation of individual struts does not set in yet. The analytical effective compressive stiffness values are then compared to the values obtained experimentally through compression testing (cf. Table 7).

Figure 9 displays the experimental results obtained by compressive testing of both bcc (a) and f2ccz (b) lattice structures for 316L stainless steel in as-built condition and Ti6Al4V before and after heat treatment. The stress–strain plots are calculated from load and displacement data based on the equivalent cross section of a homogenized solid material, with the gauge length being equivalent to the size of the lattice structure. The curves in general show the characteristic deformation behavior of stretch- and bending-dominated lattice structures at early stages of deformation [45], with the former clearly showing higher stiffness and strength than the latter. For the 316L specimens, a very ductile behavior is observed as can be deduced from the steadily increasing load bearing capacity and the absence of specimen rupture until the end of mechanical testing at 35% strain. In contrast, the Ti6Al4V lattices show a more brittle behavior with an abrupt decrease of the load carrying capability after a first maximum is reached, pointing at the sudden rupture of several struts. In the course of further loading, the typical compaction sets in and a new load carrying cycle is observed for the bcc lattice structure, cf. [39]. The load of the f2ccz structure remains on a rather constant level, indicating severe damage of the structure. After heat treatment of the Ti6Al4V specimens, improved ductility is gained, which can be seen by the smoother stress–strain graphs of the heat-treated structures. Especially in the case of the heat-treated f2ccz structure, the load drop is not as steep as prior to the heat treatment, so that a fairly damage tolerant behavior is achieved. However, the general deformation characteristics are similar to the as-built condition.

A much higher effective compressive stiffness for f2ccz lattices is observed in comparison to the bcc structures, which can be expected from the respective deformation mechanism (stretching-dominated vs. bending-dominated). The differences in aspect ratios being characteristic for the considered lattice types are listed in Table 5; however, the differences in aspect ratios here play a minor role only.

The experimental effective compressive stiffness in the build direction E^*_{exp} and the relative deviation Δ in comparison with the analytical data are listed in Table 7. The comparison with the analytical model points at absolute values of deviations in the range of 9% to 17% for the bcc lattice structures, while higher absolute deviations ranging from 20% to 70% are found for the f2ccz lattice

structures. Most effective compressive stiffness values are overestimated by the analytical model with the exception of the Ti6Al4V bcc lattice structure.

Table 5. Experimentally determined RVE sizes and strut diameters and related aspect ratios for all types of lattice specimens considered.

Material-System	RVE Size a (mm)	Strut Diameter t (mm)	Aspect Ratio AR (–)
316L-bcc	1.93	0.314	6.146
316L-f2ccz	1.81	0.371	4.879
Ti6Al4V-bcc	2.06	0.424	4.858
Ti6Al4V–f2ccz	2.04	0.399	5.113

Table 6. Results obtained by the analytical model.

Material-System	E^*_{ana} (MPa)	σ^*_{yield} (MPa)
316L-bcc	367	2.38
316L-f2ccz	8849	20.51
Ti6Al4V-bcc	463	4.75
Ti6Al4V-f2ccz	4150	18.36

Table 7. Experimental results in comparison to the analytical values providing for calculation of relative deviation.

Material-System	E^*_{exp} (MPa)	E^*_{ana} (MPa)	Δ (%)
316L-bcc	339	367	−7.6
316L-f2ccz	2824	8849	−68.1
Ti6Al4V-bcc	542	463	17.1
Ti6Al4V-bcc-HT	504		8.9
Ti6Al4V-f2ccz	3296	4150	−20.6
Ti6Al4V-f2ccz-HT	3113		−25.0

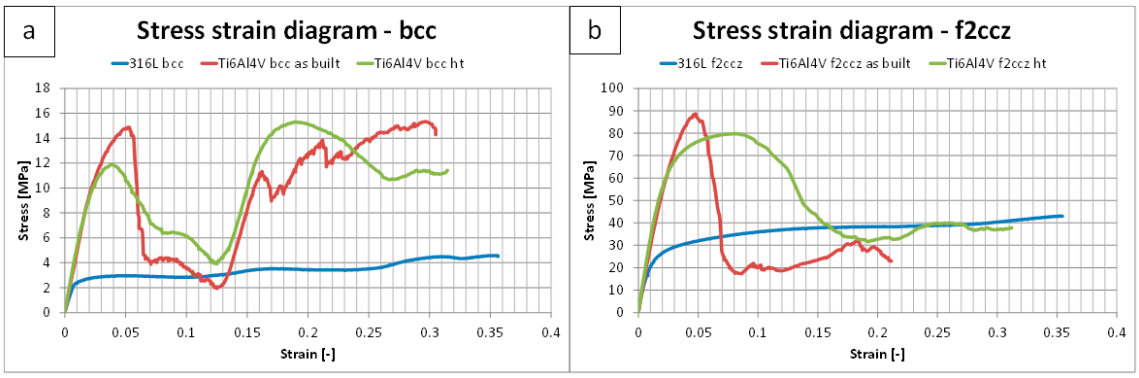

Figure 9. Experimental results–representative stress–strain diagram for all types of lattice structures obtained by compression testing, partly recompiled from [35–39,46].

In terms of effective compressive stiffness, most important influencing factors are expected to be the aspect ratio and the resulting Young's modulus. Thus, already small deviations in the assessment of the aspect ratio can lead to high deviations upon analytical determination of mechanical properties. As becomes obvious by comparing Tables 5 and 6, slightly lower aspect ratios in the case of the Ti6Al4V bcc-structures are able to compensate for the lower Young's modulus of this alloy in comparison to the 316L counterpart. Eventually, a higher stiffness in the Ti6Al4V than in the 316L bcc-structure is obtained

analytically and confirmed experimentally. As a basis for solid discussion, it is therefore necessary to determine to which level an aspect ratio effect prevails, i.e., if deviations shown in Table 6 are mostly due to measurement uncertainty that can be represented by a tolerance interval. The tolerance interval of the analytical model results is, as detailed before, determined by the precision of the measurement of dimensions related to the cell structures. In the case of the present investigation, the precision of the strut diameter determination via optical micrographs Δ_m is estimated on a conservative basis. A value of 17.5 µm, which is the difference between the minimum and maximum values of the strut diameters found, is considered for the following calculations. The tolerance interval is then obtained providing a lower and upper boundary for the estimation of the effective compressive stiffness values as follows:

$$\begin{aligned} E^*_{ana,low} &= E\left(\tfrac{a-\Delta_m}{t+\Delta_m}\right) \\ E^*_{ana,up} &= E\left(\tfrac{a+\Delta_m}{t-\Delta_m}\right) \end{aligned} \tag{1}$$

where a and t are the cell size and the strut thickness, respectively, directly deduced from the raw DIC pictures. They provide the AR of the considered RVE eventually enabling a direct correlation with the analytical stiffness of the lattice structure for the upper and lower boundary.

The deviations, for which the obtained experimental stiffness values are considered as covered by the analytical model, are expected to be within the following boundaries:

$$\begin{aligned} \Delta E^*_{ana,low} &= \tfrac{E^*_{ana}-E^*_{ana,low}}{E^*_{ana}} \\ \Delta E^*_{ana,up} &= \tfrac{E^*_{ana}-E^*_{ana,up}}{E^*_{ana}} \end{aligned} \tag{2}$$

Table 8 shows the estimated tolerance interval boundaries as calculated by Equations (1) and (2). The difference between analytical prediction and experimental result with deviations from 7% to 17% for bcc lattice structures (Table 7) are within the tolerance interval. However, the deviations obtained for the f2ccz lattices cannot be explained by possible measurement errors only, in particular for 316L showing a deviation of about 70%. However, the value of the Ti6Al4V f2ccz lattice structure in the as-built state (about 20%) is not too far off the defined tolerance band.

Table 8. Tolerance interval boundaries of the analytical model.

Material-System	$E^*_{ana,low}$ (MPa)	$\Delta E^*_{ana,low}$ (%)	$E^*_{ana,up}$ (MPa)	$\Delta E^*_{ana,up}$ (%)
316L-bcc	285	28.8	467	−21.4
316L-f2ccz	7724	14.6	10,093	−12.3
Ti6Al4V-bcc	383	20.9	556	−16.7
Ti6Al4V-f2ccz	3665	13.2	4683	−11.4

4. Discussion

The discrepancies between analytical and experimental results can partly be explained based on the limits of the model used for the calculation of the mechanical properties. Beam models account for an ideally constant cross section, while in reality the additive manufactured lattice structures tend to have relatively high variation in their cross section dimensions up to 40% [13,20,47], in particular in the area of the node intersection between several struts, resulting in locally varying stiffness and stress concentration [30,34]. An increased joint connectivity may, thus, lead to less accurate results due to the fact that the assumptions of the beam theory are locally not fulfilled in the node area. Rehme [48] and Merkt [49] performed studies focusing on the comparison of data between their analytical models and experimental results. Experimental data were acquired for several lattice structures made of 316L stainless steel using a contour hatch exposure (Rehme [48]) and point exposure strategy (Merkt [49]), respectively. Souza et al. [11] discussed that the formulation of shear loading used in the beam model applied may not be appropriate for low aspect ratios, for which the vicinity between strut-joints would

render the beam theory obsolete. It was concluded in their study that in this case the structure should be considered as a porous solid. It was highlighted that the beam model is able to predict the structural behavior with less than 20% relative error for aspect ratios above 3.8. However, much higher deviations, i.e., more than 50%, could be revealed for the smaller aspect ratios. Other potential sources of error in the analytical model can be related to the level of (in) accuracy of the input data required, i.e., the aspect ratio and the bulk material properties in the present case. The logarithmic dependency of the stiffness with regard to the aspect ratio [11] pinpoints a non-negligible impact of inaccurate measurements. A pronounced impact can be already derived from the upper and lower analytical values detailed in Table 8. Furthermore, use of values of conventional materials as a basis for the homogenisation method promotes non-exact estimation of the lattice mechanical behaviour because of the difference between conventional and additively manufactured material [50].

Moreover, defects such as porosity, surface topography and unmelted material volumes, respectively, are not taken into account, even if these features cause a change in the effective cross section [13,15], which eventually can lead to a significant decrease of the macroscopic lattice stiffness and to superposed notch effects. Geometrical discrepancies between the designed and as-built lattices are well-known and widely reported. These discrepancies can be induced by several aspects, e.g., the inclination angles of single struts [18,29,33], process instabilities [15,51], resolution limits [52] etc. As is schematically highlighted in Figure 10, bcc lattice structures offer a layer-wise regular periodic pattern with only one orientation (taking into account symmetry of the four struts highlighted), while the f2ccz periodical arrangement displays a lesser degree of homogeneity of the lattice pattern due to an additional and, in the case of tension/compression loading, load carrying vertical strut. Known effects such as wall thickness variation and strut waviness can be considered as variables depending on the strut inclination finally impacting the mechanical behavior of the lattice structure. Due to the dominant contribution of one single type of strut orientation to the overall performance of the f2ccz lattice structure, it is expected that the f2ccz structure is subjected to higher variations in terms of mechanical properties than the bcc lattice structures. This effect can be clearly seen in Table 7.

However, these arguments solely do not explain the high variance in the deviations observed between experimental and analytical results in the present work, up to almost 70% in the particular case of the 316L alloy. The critical value, below which the lattice has to be contemplated as a porous solid, is not touched in case of the structures investigated in this paper. Rehme [48] concluded that the transition from a lattice structure, i.e., a truss-structure composed of single struts, to a porous solid has to be defined according to the relevant aspect ratio. According to Table 5, the aspect ratios obtained in the present study are in between 4 and 6. According to literature, the lower aspect ratio bound is around 1.63 for bcc and 2.414 for f2ccz lattice structures [11,48]. From data presented, it is obvious that both f2ccz lattice structures, independent of the material considered, exhibit significantly higher deviations than their bcc counterparts, the latter being characterised by a lower grade of joint connectivity. This observation clearly confirms the already mentioned limits of the approach considered, i.e., modelling struts as structural beam elements. It is also quite remarkable that the stiffness prediction for bcc structures remains below 10% inaccuracy for materials with potential industrial application (316L, Ti6Al4V HT). Furthermore, an overall better correlation for specimens made from Ti6Al4V can be identified, for which the calculated stiffness can be assumed as absolutely acceptable since values remain in the tolerance interval detailed in Table 8.

For the 316L alloy, the vertically built struts show a strong dependency of both texture and grain size towards their diameter. With decreasing diameter, changes from a rather fine, globular and weakly textured microstructure to a coarse, elongated and strongly textured microstructure are seen (Figure 5). This miniaturisation phenomenon can be explained through changes in the solidification conditions, the prevailing temperature gradients and the overall thermal history of a given volume element. Details on fundamental solidification effects and the impact of rapid solidification on microstructure evolution can be found in literature, e.g., [53,54]. In case of additive manufacturing, geometry and microstructure are established in parallel. Thus, changes in geometrical features on a

given plane of view (cf. Figure 10) are directly connected to the scanning strategy within the given layer, eventually affecting very important process inherent characteristics such as the return time, i.e., the time interval between irradiation of two strongly overlapping volume elements of the structure. This can lead to significant changes of the melt pool shape, temperatures in the top layer and other process characteristics. This, for one thing, leads to a change of solidification velocity and, thus, change of prevalent grain sizes. Furthermore, in the case of miniaturisation of structural elements, the thermal gradient is strongly directed towards the building platform, as the heat can only be dissipated through the layers underneath, i.e., the already solidified material (as its thermal conductivity is much higher as in case of the loose powder), cf. Figure 11. In combination with the driving force imposed by epitaxial grain growth, this results in a strong <001> texture and grains being significantly higher in length (parallel to BD) than the powder layer thicknesses employed in the process. Such aspects have been numerously reported in literature, e.g., by Thijs et al. for additive processed tantalum [24]. For bigger cross sections, the return times can be much longer, while the local heat is effectively distributed in the solid material surrounding the melt pool, promoting the typically observed microstructure for additive manufactured material (as shown in Figures 5 and 11 for the specimens with diameters of 3.1 mm and 5 mm). All the aforementioned aspects are highly relevant for miniaturised, thin walled lattice structures. In the case of the two different lattice types considered, different cross section patterns are exposed as shown schematically in Figure 10. Consequently, the strut inclination angle does not only have an impact on the geometrical discrepancies discussed before, but also leads to slightly different microstructures in each strut. Similar conclusions were reported for additively manufactured notch specimens made from stainless steel 316L, where a strong impact of ligament dimensions on locally prevailing microstructure and eventually mechanical properties was reported [21].

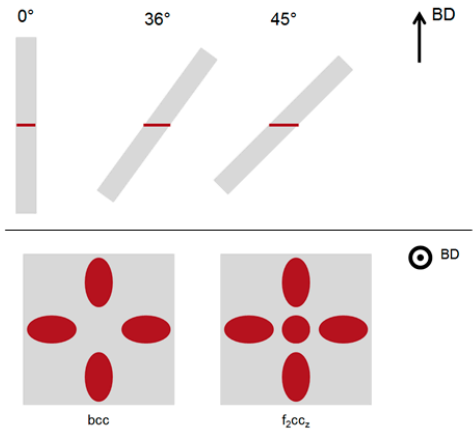

Figure 10. Irradiated cross sections of bcc and f2ccz lattice structures for an arbitrary layer highlighting the impact of strut inclination.

These microstructural changes, i.e., stronger <001> texture [35,36] and increased grain size with respect to the build direction, significantly reduce both Young's modulus and yield strength, as has been shown for bulk 316L in a previous study [21]. In consequence, a lower stiffness and yield strength can also be expected in lattice structures of small geometrical dimensions, as long as their deformation behavior under tensile or compressive loading is dominated by small, vertically built struts. As is revealed by analysis of DIC data shown in Figure 7, this is exactly the case for the 316L f2ccz structure. Thus, the high deviation between the analytically determined and the experimentally obtained results for this structure can be related to a significant reduction of stiffness and strength of the load carrying struts oriented parallel to the loading direction. It can be unambiguously concluded that, as long as tensile/compressive loading dominate, the miniaturisation effect is decisive, as revealed in the present study for the f2ccz structure. In contrast, if the deformation behavior is dominated by bending, the anisotropic properties are not as highly effective, as multiaxial stress states are induced within the

struts. For the bcc lattice structure, displaying a superposition of compressive and bending forces (cf. Figure 7d–f), the miniaturisation effect is, thus, less influential for the structure as compared to the impact of the overall geometry. Consequently, the deviation between analytical and experimental results is much smaller.

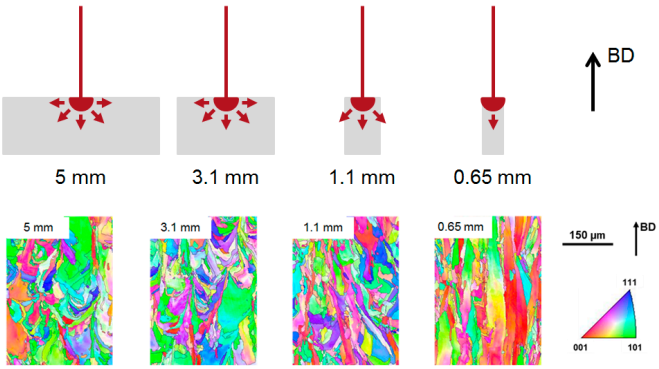

Figure 11. Schematic highlighting the interrelations of meltpool size, heat flux, and resulting microstructure for geometries being characterised by miniaturised dimensions. Interrelations hold true for materials not showing any phase transformation upon solidification, partly recompiled from [38].

It has to be noted that the discussed relationships between geometrical dimensions, solidification conditions, microstructure evolution and resulting mechanical properties are most effective only for materials, which still feature their solidification microstructure at room temperature. This is obviously not the case for Ti6Al4V (Figure 6), as this alloy undergoes an additional solid-to-solid phase transformation from the cubic β-phase (the high-temperature solidification phase) to α-martensite, imposed by rapid cooling and quenching, respectively, upon solidification. During the transformation, the strong texture and coarse-grained microstructure of the former β-phase is almost fully lost and a very fine-grained, weakly textured martensite is formed. Only selection of preferred martensite variants resembles the initial microstructural features, e.g., the lateral position of former β-phase grain boundaries [25]. Thus, the behavior of both bcc and f2ccz structures in the as-built condition of Ti6Al4V is not affected by locally prevailing anisotropic microstructures. That is why the experimentally determined stiffness values of both structure types are within or close to the tolerance band of the analytical model. A higher deviation between the analytically and experimentally determined stiffness values for the heat-treated Ti6Al4V lattice, as compared to the as-built counterparts, can be deduced for the f2ccz structure only. As in case of the 316L specimens, this is the type of structure where microstructural effects are more prominent due to the uniaxial stress states within the load carrying struts. For Ti6Al4V, grain coarsening induced by the heat treatment might lead to local reduction of stiffness in dependence of the local grain orientation. However, as the grain coarsening is induced by recovery, grain growth and recrystallization, the orientation cannot be controlled and, thus, countervailing effects of individual grains on the resulting stiffness can be assumed. However, this aspect is clearly out of the scope of the current work and, thus, has to be addressed in a follow-up study.

5. Conclusions

The general performance of an additively manufactured part is defined by the process parameters locally applied and the evolution of microstructure induced eventually determining its local and global mechanical behavior. In the case of lattice structures, the macroscopic mechanical properties are expected to be highly influenced by the type of lattice involved, i.e., by effects on the macro- and mesoscale, however, simultaneously by the different grain orientations and textures, respectively, on the microscale. All these aspects are characterised by their own individual parameters and variables, however, all being cross-linked. It is assumed that properties on each length scale have to be investigated separately first. Then, upon fusion of results, an explicit statement can be provided, allowing for solid

conclusion regarding the general behavior of the structures considered. Finally, this approach allows for transfer of results to closely related lattices, e.g., characterised by similar geometry, however, differing dimensions.

The multi-scale analysis of the present study reveals that the miniaturisation effect has a distinct, however, different impact on the deformation behavior of lattice structures depending on the considered type of the unit cell, the loading scenario and the material of choice. Materials subjected to a phase change upon solidification, such as Ti6Al4V, are less sensitive due to local microstructural changes inhibiting the miniaturisation effect, which enables accurate prediction of the mechanical behaviour using constitutive models for structures with few manufacturing defects. Other common additive manufacturing materials such as 316L, Ni-base alloys [55], and AlSi10Mg [56] are strongly impacted by the miniaturisation effect. This effect, among others, is generally not taken into account in analytical or finite element models, where typically isotropic and size-independent properties are assumed. The direct consequence of these inadequate assumptions is an overestimation of the structural properties. This clearly lays out that the so far developed models may not be conservative, being further characterized by extremely high deviations from real structural data.

Author Contributions: Conceptualization and methodology, G.M. and F.B.; validation, T.N. and C.M.; formal analysis, G.M. and F.B.; investigation, F.B.; data curation, G.M.; writing—original draft preparation, G.M.; writing—review and editing, G.M., F.B., T.N., and C.M.; visualization, G.M.; supervision and project administration, T.N. and C.M. All authors have read and agreed to the published version of the manuscript.

Funding: Financial support by Deutsche Forschungsgemeinschaft (Project No. 250216343; NI1327/7-3).

Acknowledgments: IfW and KluB acknowledge the financial support by Deutsche Forschungsgemeinschaft and provision of machine time for L-PBF processing by DMRC (University of Paderborn) gratefully. The authors thank all reviewers for their constructive recommendations and useful suggestions.

Conflicts of Interest: The authors declare no conflict of interest.

References

1. Verein Deutscher Ingenieure. *Konstruktionsempfehlungen für die Bauteilfertigung mit Laser-Sintern und Laser-Strahlschmelzen*; VDI-Richtlinie 3405 Blatt 3; Verein Deutscher Ingenieure: Düsseldorf, Germany, 2014.
2. Richard, H.A.; Schramm, B.; Zipsner, T. *Additive Fertigung von Bauteilen und Strukturen*; Springer Science and Business Media LLC: Berlin, Germany, 2017.
3. Schmidt, T. *Potentialbewertung Generativer Fertigungsverfahren für Leichtbauteile*; Springer Science and Business Media LLC: Berlin, Germany, 2016.
4. Yusuf, S.M.; Cutler, S.; Gao, N. Review: The Impact of Metal Additive Manufacturing on the Aerospace Industry. *Metals* **2019**, *9*, 1286. [CrossRef]
5. Gebhardt, A.; Hötter, J.S. *Additive Manufacturing 3D Printing for Prototyping and Manufacturing*; Carl Hanser Verlag: München, Germany, 2016.
6. Maconachie, T.; Leary, M.; Lozanovski, B.; Zhang, X.; Qian, M.; Faruque, O.; Brandt, M. SLM lattice structures: Properties, performance, applications and challenges. *Mater. Des.* **2019**, *183*, 108137. [CrossRef]
7. Ashby, M.F. The properties of foams and lattices. *Philos. Trans. R. Soc. A Math. Phys. Eng. Sci.* **2005**, *364*, 15–30. [CrossRef] [PubMed]
8. Vigliotti, A.; Deshpande, V.S.; Pasini, D. Non linear constitutive models for lattice materials. *J. Mech. Phys. Solids* **2014**, *64*, 44–60. [CrossRef]
9. Bonatti, C.; Mohr, D. Large deformation response of additively-manufactured FCC metamaterials: From octet truss lattices towards continuous shell mesostructures. *Int. J. Plast.* **2017**, *92*, 122–147. [CrossRef]
10. Messner, M.C. Optimal lattice-structured materials. *J. Mech. Phys. Solids* **2016**, *96*, 162–183. [CrossRef]
11. Souza, J.; Großmann, A.; Mittelstedt, C. Micromechanical analysis of the effective properties of lattice structures in additive manufacturing. *Addit. Manuf.* **2018**, *23*, 53–69. [CrossRef]
12. Van Bael, S.; Kerckhofs, G.; Moesen, M.; Pyka, G.; Schrooten, J.; Kruth, J. Micro-CT-based improvement of geometrical and mechanical controllability of selective laser melted Ti6Al4V porous structures. *Mater. Sci. Eng. A* **2011**, *528*, 7423–7431. [CrossRef]

13. Dressler, A.D.; Jost, E.W.; Miers, J.C.; Moore, D.G.; Seepersad, C.C.; Boyce, B.L. Heterogeneities dominate mechanical performance of additively manufactured metal lattice struts. *Addit. Manuf.* **2019**, *28*, 692–703. [CrossRef]
14. Qiu, C.; Yue, S.; Adkins, N.J.; Ward, M.; Hassanin, H.; Lee, P.D.; Withers, P.J.; Attallah, M.M. Influence of processing conditions on strut structure and compressive properties of cellular lattice structures fabricated by selective laser melting. *Mater. Sci. Eng. A* **2015**, *628*, 188–197. [CrossRef]
15. Liu, L.; Kamm, P.; García-Moreno, F.; Banhart, J.; Pasini, D. Elastic and failure response of imperfect three-dimensional metallic lattices: The role of geometric defects induced by Selective Laser Melting. *J. Mech. Phys. Solids* **2017**, *107*, 160–184. [CrossRef]
16. Sing, S.L.; Wiria, F.E.; Yeong, W.Y. Selective laser melting of lattice structures: A statistical approach to manufacturability and mechanical behavior. *Robot. Comput. Manuf.* **2018**, *49*, 170–180. [CrossRef]
17. Tsopanos, S.; Mines, R.; McKown, S.; Shen, Y.; Cantwell, W.J.; Brooks, W.; Sutcliffe, C.J. The Influence of Processing Parameters on the Mechanical Properties of Selectively Laser Melted Stainless Steel Microlattice Structures. *J. Manuf. Sci. Eng.* **2010**, *132*, 041011. [CrossRef]
18. Leary, M.; Mazur, M.; Elambasseril, J.; McMillan, M.; Chirent, T.; Sun, Y.; Qian, M.; Easton, M.; Brandt, M. Selective laser melting (SLM) of AlSi12Mg lattice structures. *Mater. Des.* **2016**, *98*, 344–357. [CrossRef]
19. Großmann, A.; Gosmann, J.; Mittelstedt, C. Lightweight lattice structures in selective laser melting: Design, fabrication and mechanical properties. *Mater. Sci. Eng. A* **2019**, *766*, 138356. [CrossRef]
20. Suard, M.; Martin, G.; Lhuissier, P.; Dendievel, R.; Vignat, F.; Blandin, J.-J.; Villeneuve, F. Mechanical equivalent diameter of single struts for the stiffness prediction of lattice structures produced by Electron Beam Melting. *Addit. Manuf.* **2015**, *8*, 124–131. [CrossRef]
21. Brenne, F.; Niendorf, T. Damage tolerant design by microstructural gradation—Influence of processing parameters and build orientation on crack growth within additively processed 316L. *Mater. Sci. Eng. A* **2019**, *764*, 138186. [CrossRef]
22. Niendorf, T.; Leuders, S.; Riemer, A.; Richard, H.A.; Tröster, T.; Schwarze, D. Highly Anisotropic Steel Processed by Selective Laser Melting. *Met. Mater. Trans. A* **2013**, *44*, 794–796. [CrossRef]
23. Thijs, L.; Verhaeghe, F.; Craeghs, T.; Van Humbeeck, J.; Kruth, J.-P. A study of the microstructural evolution during selective laser melting of Ti-6Al-4V. *Acta Mater.* **2010**, *58*, 3303–3312. [CrossRef]
24. Thijs, L.; Sistiaga, M.L.M.; Wauthle, R.; Xie, Q.; Kruth, J.-P.; Van Humbeeck, J. Strong morphological and crystallographic texture and resulting yield strength anisotropy in selective laser melted tantalum. *Acta Mater.* **2013**, *61*, 4657–4668. [CrossRef]
25. Antonysamy, A.; Meyer, J.; Prangnell, P. Effect of build geometry on the β-grain structure and texture in additive manufacture of Ti6Al4V by selective electron beam melting. *Mater. Charact.* **2013**, *84*, 153–168. [CrossRef]
26. Niendorf, T.; Brenne, F.; Schaper, M.; Riemer, A.; Leuders, S.; Reimche, W.; Schwarze, D.; Maier, H.J. Labelling additively manufactured parts by microstructural gradation–advanced copy-proof design. *Rapid Prototyp. J.* **2016**, *22*, 630–635. [CrossRef]
27. Ishimoto, T.; Hagihara, K.; Hisamoto, K.; Sun, S.H.; Nakano, T. Crystallographic texture control of beta-type Ti-15Mo-5Zr-3Al alloy by selective laser melting for the development of novel implants with a biocompatible low Young's modulus. *Scrpitamat* **2017**, *132*, 34–38. [CrossRef]
28. Kurzynowski, T.; Gruber, K.; Stopyra, W.; Kuźnicka, B.; Chlebus, E. Correlation between process parameters, microstructure and properties of 316 L stainless steel processed by selective laser melting. *Mater. Sci. Eng. A* **2018**, *718*, 64–73. [CrossRef]
29. Dong, Z.; Liu, Y.; Zhang, Q.; Ge, J.; Ji, S.; Li, W.; Liang, J. Microstructural heterogeneity of AlSi10Mg alloy lattice structures fabricated by selective laser melting: Phenomena and mechanism. *J. Alloys Compd.* **2020**, *833*, 155071. [CrossRef]
30. Dong, Z.; Liu, Y.; Li, W.; Liang, J. Orientation dependency for microstructure, geometric accuracy and mechanical properties of selective lase melting AlSi10Mg lattices. *J. Alloys Compd.* **2019**, *791*, 490–500. [CrossRef]
31. Tancogne-Dejean, T.; Spierings, A.B.; Mohr, D. Additively-manufactured metallic micro-lattice materials for high specific energy absorption under static and dynamic loading. *Acta Mater.* **2016**, *116*, 14–28. [CrossRef]

32. Wauthle, R.; Vrancken, B.; Beynaerts, B.; Jorissen, K.; Schrooten, J.; Kruth, J.-P.; Van Humbeeck, J. Effects of build orientation and heat treatment on the microstructure and mechanical properties of selective laser melted Ti6Al4V lattice structures. *Addit. Manuf.* **2015**, *5*, 77–84. [CrossRef]
33. Delroisse, P.; Jacques, P.J.; Maire, E.; Rigo, O.; Simar, A. Effect of strut orientation on the microstructure heterogeneities in AlSi10Mg lattices processed by selective laser melting. *Scr. Mater.* **2017**, *141*, 32–35. [CrossRef]
34. Huynh, L.; Rotella, J.; Sangid, M.D. Fatigue behavior of IN718 microtrusses produced by additive manufacturing. *Mater. Des.* **2016**, *105*, 278–389. [CrossRef]
35. Brenne, F. *Selektives Laserschmelzen Metallischer Materialien: Einfluss von Prozessparametern und Miniaturisierung auf Mikrostruktur und Mechanisches Verhalten Geometrisch Komplexer Strukturen*; Kassel University: Kassel, Germany, 2018.
36. Wang, X.; Muñiz-Lerma, J.A.; Sánchez-Mata, O.; Shandiz, M.A.; Brochu, M. Microstructure and mechanical properties of stainless steel 316L vertical struts manufactured by laser powder bed fusion process. *Mater. Sci. Eng. A* **2018**, *736*, 27–40. [CrossRef]
37. Brenne, F.; Niendorf, T.; Maier, H. Additively manufactured cellular structures: Impact of microstructure and local strains on the monotonic and cyclic behavior under uniaxial and bending load. *J. Mater. Process. Technol.* **2013**, *213*, 1558–1564. [CrossRef]
38. Niendorf, T.; Brenne, F.; Schaper, M. Lattice structures manufactured by SLM–On the effect of geometrical dimensions on microstructure evolution during processing. *Metall. Mater. Trans. B* **2014**, *45*, 1181–1185. [CrossRef]
39. Brenne, F.; Niendorf, T. Load distribution and damage evolution in bending and stretch dominated Ti-6Al-4V cellular structures processed by selective laser melting. *Int. J. Fatigue* **2019**, *121*, 219–228. [CrossRef]
40. Gorny, B.; Niendorf, T.; Lackmann, J.; Thoene, M.; Troester, T.; Maier, H. In situ characterization of the deformation and failure behavior of non-stochastic porous structures processed by selective laser melting. *Mater. Sci. Eng. A* **2011**, *528*, 7962–7967. [CrossRef]
41. Timoshenko, S.P.; Gere, J.M.; Prager, W. Theory of Elastic Stability, Second Edition. *J. Appl. Mech.* **1962**, *29*, 220–221. [CrossRef]
42. Röttger, A.; Boes, J.; Theisen, W.; Thiele, M.; Esen, C.; Edelmann, A.; Hellmann, R. Microstructure and mechanical properties of 316L austenitic stainless steel processed by different SLM devices. *Int. J. Adv. Manuf. Technol.* **2020**, *108*, 769–783. [CrossRef]
43. Karolewska, K.; Ligaj, B.; Wirwicki, M.; Szala, G. Strength analysis of Ti6Al4V titanium alloy produced by the use of additive manufacturing method under static load conditions. *J. Mater. Res. Technol.* **2020**, *9*, 1365–1379. [CrossRef]
44. Leuders, S.; Thöne, M.; Riemer, A.; Niendorf, T.; Troster, T.; Richard, H.; Maier, H. On the mechanical behaviour of titanium alloy TiAl6V4 manufactured by selective laser melting: Fatigue resistance and crack growth performance. *Int. J. Fatigue* **2013**, *48*, 300–307. [CrossRef]
45. Mazur, M.; Leary, M.; Sun, S.; Vcelka, M.; Shidid, D.; Brandt, M. Deformation and failure behaviour of Ti-6Al-4V lattice structures manufactured by selective laser melting. *Int. J. Adv. Manuf. Technol.* **2016**, *84*, 1391–1411. [CrossRef]
46. Niendorf, T.; Brenne, F.; Maier, H.J. Damage evolution in truss structures manufactured by selective laser melting–effect of loading conditions. In Proceedings of the CELLMAT 2012, Dresden, Germany, 7–9 November 2012.
47. Boniotti, L.; Beretta, S.; Patriarca, L.; Rigoni, L.; Foletti, S. Experimental and numerical investigation on compressive fatigue strength of lattice structures of AlSi7Mg manufactured by SLM. *Int. J. Fatigue* **2019**, *128*, 105181. [CrossRef]
48. Rehme, O. *Cellular Design for Laser Freeform Fabrication*, 1st ed.; Vol. v.4 of Schriftenreihe Lasertechnik; Cuvillier Verlag: Göttingen, Germany, 2010.
49. Merkt, S.; Klocke, F. *Qualifizierung von Generativ Gefertigten Gitterstrukturen für maßgeschneiderte Bauteilfunktionen*; RWTH Aachen: Aachen, Germany, 2015.
50. Said, J.M.; Ismail, M.H.; Abidin, N.A.Z.; Haris, N.A.; Roslan, A.N.M. Additive Manufacturing of 316L Stainless Steel. *Int. J. Recent Technol. Eng.* **2019**, *8*, 6825–6829. [CrossRef]
51. Olakanmi, E. Selective laser sintering/melting (SLS/SLM) of pure Al, Al–Mg, and Al–Si powders: Effect of processing conditions and powder properties. *J. Mater. Process. Technol.* **2013**, *213*, 1387–1405. [CrossRef]

52. Reu, P.L.; Sweatt, W.; Miller, T.; Fleming, D. Camera System Resolution and its Influence on Digital Image Correlation. *Exp. Mech.* **2014**, *55*, 9–25. [CrossRef]
53. Kurz, W.; Fisher, D. *Fundamentals of Solidification*; Trans Tech Publ. Ltd.: Weinheim, Germany, 1998. [CrossRef]
54. Gäumann, M.; Henry, S.; Cléton, F.; Wagnière, J.-D.; Kurz, W. Epitaxial laser metal forming: Analysis of microstructure formation. *Mater. Sci. Eng. A* **1999**, *271*, 232–241. [CrossRef]
55. Kotzem, D.; Arold, T.; Niendorf, T.; Walther, F. Damage Tolerance Evaluation of E-PBF-Manufactured Inconel 718 Strut Geometries by Advanced Characterization Techniques. *Materials* **2020**, *13*, 247. [CrossRef]
56. Takata, N.; Kodaira, H.; Suzuki, A.; Kobashi, M. Size dependence of microstructure of AlSi10Mg alloy fabricated by selective laser melting. *Mater. Charact.* **2018**, *143*, 18–26. [CrossRef]